Electrical Power and Energy Systems 77 (2016) 112–122

Contents lists available at ScienceDirect

Electrical Power and Energy Systems

journal homepage: www.elsevier.com/locate/ijepes

An improved control scheme for grid connected doubly fed induction generator considering wind-solar hybrid system

Adikanda Parida *, Debashis Chatterjee [1]

Department of Electrical Engineering, Jadavpur University, Kolkata, India

ARTICLE INFO

Article history:
Received 26 September 2014
Received in revised form 29 May 2015
Accepted 17 November 2015

Keywords:
Doubly fed induction generator
Wind-solar hybrid system
Parameter sensitivity
Rotor position estimation
Model reference adaptive system

ABSTRACT

This paper proposes a wind-solar hybrid generation scheme, along with an improved control strategy for grid connected wind energy conversion system (WECS) considering parameter uncertainty. In the proposed scheme, a photo voltaic (PV) supplemented rotor power management scheme (RPMS) has been developed for doubly fed induction generator (DFIG) with stator connected to grid. The topology of RPMS is implemented in isolation with the grid during entire period of DFIG operation. The proposed scheme ensures an increased output power delivered to the grid during low wind speeds. The DFIG control scheme require accurate information for the rotor position and speed at all operating conditions, which is estimated in the proposed method without any significant dependency on machine parameters. The control strategy proposed in this paper is implemented with a 2.5 kW DFIG using dSPACE DS1104 module with PC interface, which produced satisfactory results.

Introduction

The wind energy shares a considerable segment amongst all the generations in the world energy scenario. At present doubly fed induction generators with suitable control scheme, provides a low cost alternative with high dynamic performance for power ranges from kW to MW for the purpose of wind energy conversion. The precise control of DFIG requires accurate information of rotor position angle and rotor speed. The rotor speed sensorless option for the control of DFIGs are more preferred due to its improved reliability, lower capital cost investment and lower maintenance. Moreover mounting of speed sensors require additional space which may not be available in some of the systems. The dual converter based controllers with sensorless estimation of rotor speed and position has been widely addressed [1–16,18–21]. The earlier control schemes are complex to coordinate and incapable to maintain the grid connectivity of DFIG at low wind speeds. Also the earlier proposed rotor speed and position estimation algorithms [1–5] are based on open loop methods, where the estimation is implemented with the use of differentiators. This can introduce error due to noise in the input signals for computation of rotor speed and position. Similar type of controller with MRAS based rotor speed and position algorithms are proposed in [6–10]. But these are directly sensitive to magnetizing inductance variations which affects the stability and reliability of the controller. The control algorithm proposed in [11] suffers from problems associated with integration at low frequency for the rotor side variables around synchronous speed. The rotor speed and position estimation techniques presented in [12–16] are based on hysteresis controllers where the adjustable model parameter is directly sensitive to the machine magnetizing inductance. A current based direct power control strategy for DFIG has been proposed in [18]. The dual converter based controllers are proposed in [19–21] under various grid disturbances. Almost all of the already proposed controllers are derived in such a way that the rotor side converter (RSC) of the machine is fed from another converter connected to grid known as grid side converter (GSC). Thus, the grid disturbances can directly affect the control of both these converters and thereby reducing grid connectivity options under these situations. Moreover, none of these techniques address the problem of grid connectivity improvement options under low wind speeds situations.

In this paper a novel wind-solar hybrid power generation scheme for grid connected DFIG has been developed considering improved connectivity option in the subsynchronous range. The continuity of supply to grid during low wind speed conditions with enhanced output power is the major advantage of the proposed scheme. The proposed scheme is implemented with only rotor side converter, thus RSC controller is working in isolation with the grid. The dc power input to the controller is provided from a PV panel along with storage battery of appropriate size. The PV panel supplements the rotor power during low wind speeds to generate

* Corresponding author. Tel.: +91 9436633939.
E-mail addresses: adikanda_2003@yahoo.co.in (A. Parida), debashisju@yahoo.com (D. Chatterjee).
[1] Tel.: +91 3324146100.

http://dx.doi.org/10.1016/j.ijepes.2015.11.036
0142-0615/

Nomenclature

$\lambda^s_{\alpha s}, \lambda^s_{\beta s}$	α–β axis components of stator flux in stationary reference frame
$v^s_{\alpha s}, v^s_{\beta s}$	α–β axis components of stator voltages in stationary reference frame
$i^s_{\alpha s}, i^s_{\beta s}$	α–β axis components of stator currents in stationary reference frame
$i^s_{\alpha r}, i^s_{\beta r}$	α–β axis components of rotor current transformed into stator reference frame
$i^r_{\alpha r}, i^r_{\beta r}$	α–β axis components of measured rotor currents in rotor reference frame
L_m, L_s, L_{ls}, L_{lr}	magnetizing, stator self, stator leakage and rotor leakage inductances of DFIG
R_s	stator resistance
T_e, p	electromagnetic torque, number of poles
ω_e, ω_r	angular velocity of stator magnetizing flux, rotational speed of rotor
θ_r	rotor position angle
σ_s	stator leakage factor
K_p, K_i	proportional constant and Integral constants of PI-controller
τ_s	time constant of the delay introduced by sampling
ω_o	electrical frequency of the machine

Subscripts

(r, s)	rotor or stator quantities

constant output power to be fed to the grid. The proposed control algorithm needs correct information regarding rotor speed and position for stability and reliability of the system. The proposed method, effectively estimates the said quantities under variable wind speed condition including near synchronous speed. The estimation process is almost independent of machine parameter variations. The proposed model for rotor position and speed estimation is stable under all loading conditions while catching the actual value of rotor speed including starting on fly. The method is simple and can be easily implemented for practical applications.

Architecture of the proposed controller

The schematic of the proposed system is shown in Fig. 1. The rotor power is controlled by a rotor side converter only, replacing the widely used dual converter scheme connected to grid. A suitable PV module assists the rotor power management system (RPMS) to maintain a constant voltage across dc-link capacitor (C_d). The diode connected in series with the solar panel protects the PV module from voltage surges and prevents reverse current flow during low irradiation periods.

The dc-bus voltage (V_{dc}) is compared with the reference dc voltage (V^*_{dc}) and the error signal is fed to a hysteresis controller which generates switching pulses for the IGBT based dc chopper circuit with help of a suitable pulse driver circuit. When $V_{dc} > V^*_{dc}$, the IGBT2 charges the battery2 for future usage and the excess energy after charging can be dumped to another auxiliary load through a switch shown in Fig. 1. The selection of capacitor and battery can be flexible as it is based on the local wind profile. When both wind and solar power is not available, the stored energy in battery2 can be utilized to provide rotor power through IGBT3.

The proposed system shown in Fig. 1 can operate in the following modes.

Mode 1: Wind power is low (subsynchronous rotor speed) and solar power is sufficient.

In this mode, the rotor power needed is supplied directly from solar panel. If the requirement of rotor power P2 is more than solar energy generated, battery1 can supply the balance power. If solar energy generated is more than rotor power P2 needed, the excess power will stored in battery1 and then in battery2.

Mode 2: Both wind and solar powers are low.

In this mode, the rotor power P2 needed is supplied from battery1 and battery2.

Mode 3: Wind power is large and solar power is low.

In this mode, the rotor goes to supersynchronous region and rotor power P2 will be extracted from the rotor. This power is directly stored both in battery1 and battery2.

Mode 4: Both wind power and solar power are high.

In this case, both the rotor power and solar power gets stored in battery1 and battey2. If the generated power is large, the dc-bus voltage will rise which enable the switch SW shown in Fig. 1 to connect to auxiliary load to utilize the excess power.

a. Generation of reference signals.

The DFIG generates power at constant voltage and constant frequency at the stator terminals irrespective of the shaft speed. In the proposed scheme, a stator flux oriented control strategy has been adopted for this purpose. For stator flux orientation with stator flux λ_s oriented along synchronously rotating d-axis, $\lambda_s = \lambda_{ds}$, thus $\lambda_{qs} = 0$. Where, $\lambda_{ds}, \lambda_{qs}$ are the d–q components of the stator flux in synchronous reference frame.

The stator flux can be expressed as [22],

$$\begin{bmatrix} \lambda_{ds} \\ \lambda_{qs} \end{bmatrix} = L_s \begin{bmatrix} i_{ds} \\ i_{qs} \end{bmatrix} + L_m \begin{bmatrix} i_{dr} \\ i_{qr} \end{bmatrix} \tag{1}$$

Where, i_{ds}, i_{qs} and i_{dr}, i_{qr} are the d–q stator and rotor currents in synchronous reference frame. Therefore, reference value of rotor currents (i^*_{dr}, i^*_{qr}) in synchronous reference frame can be computed using (1) as,

$$i^*_{qr} = -(L_s/L_m) i_{qs}, \quad i^*_{dr} = (1/L_m)\lambda_{ds} - (L_s/L_m) i_{ds} \tag{2}$$

The rotor voltage equations in synchronous reference frame is given by [23],

$$\begin{bmatrix} v_{dr} \\ v_{qr} \end{bmatrix} = Rr \begin{bmatrix} i_{dr} \\ i_{qr} \end{bmatrix} + (d/dt) \begin{bmatrix} \lambda_{dr} \\ \lambda_{qr} \end{bmatrix} + \omega_{slip} \begin{bmatrix} -\lambda_{qr} \\ \lambda_{dr} \end{bmatrix} \tag{3}$$

The d–q axis rotor voltage references (V^*_{dr}, V^*_{qr}) can be expressed with the stator flux orientation of d-axis utilizing (1) and (3) as,

$$V^*_{dr} = V'_{dr} - (\omega_{slip})\sigma L_r i_{qr} \tag{4}$$

$$V^*_{qr} = V'_{qr} + (\omega_{slip})\left(\left(L^2_m/L_s\right) i_{ms} + \sigma L_r i_{dr}\right) \tag{5}$$

Where ω_{slip} is the slip speed, $\sigma = \left(1 - \frac{L^2_m}{L_s L_r}\right)$ is the leakage factor, i_{ms} is the magnetizing current and V'_{dr}, V'_{qr} are the control outputs of PI controllers PI_1 and PI_2 respectively as shown in Fig. 1. The PI controller outputs V'_{dr}, V'_{qr} are used to generate rotor d–q axes voltage reference using (4) and (5).

The control of rotor-side PWM converter requires the measurement of the stator voltage and current and rotor current.

b. Power flow.

The DFIG power flow diagram is shown in Fig. 2a for existing conventional scheme of rotor side converter connected to grid and in Fig. 2b for the proposed scheme. Different power

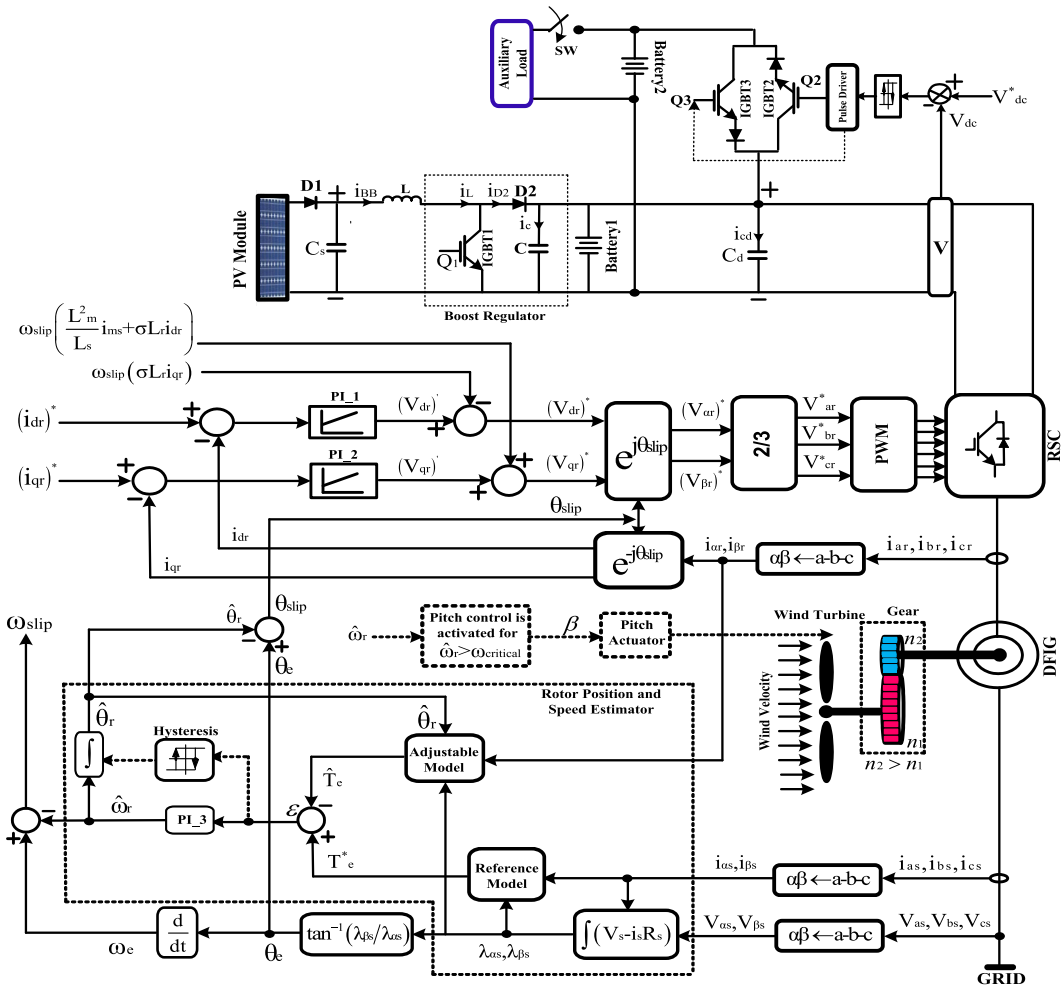

Fig. 1. Proposed scheme of the wind energy conversion system.

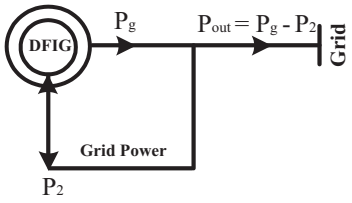

Fig. 2a. Power flow in conventional scheme.

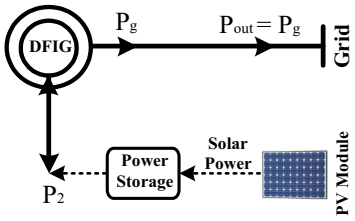

Fig. 2b. Power flow in proposed scheme.

components of the generator that are indicated in Figs. 2b and 2c are P_g, P_2 and P_{out}. The rotor power is represented as P_2 and the air gap power crossing the rotor is indicated by P_g. The net output power, which is fed to the grid is represented as P_{out} which is equal to P_g for the proposed scheme when all stator losses are neglected. With 's' signify the generator slip, the rotor side power relationship can be expressed as,

$$sP_g = P_2 + P_{cur} \tag{6}$$

where P_{cur} is the rotor cupper loss. For subsynchronous operation, which is of present interest, the slip $s > 0$. Again for generator action P_g will be always negative and thus $P_g < 0$. Therefore, $sP_g < 0$. Again from (6), when $sP_g < 0, P_2 + P_{cur} < 0$. As P_{cur} is always positive, it can be concluded that $P_2 < 0$. Indicating the shaft mechanical power input for the DFIG as P_m, the relationship between P_m and P_g can be expressed as,

$$P_m = P_g(1 - s) \tag{7}$$

Therefore, from (6) and (7),

$$P_g = P_m + P_2 + P_{cur} \tag{8}$$

Thus from (8) with P_m and P_g negative for generator operation and P_2 negative in sub-synchronous region, $|P_g| > |P_2|$. Hence it can be concluded that available electrical power at stator terminals (P_g) will be always greater than the electrical injected power (P_2) at the rotor side.

For the given machine with specifications shown in Appendix A, experiments were conducted at the sub-synchronous region with varying the rotor speed between 1350 rpm to 450 rpm. The rotor injected power P_2 is measured at the dc-bus as $P_2 = V_{dc}.i_{dc}$. The

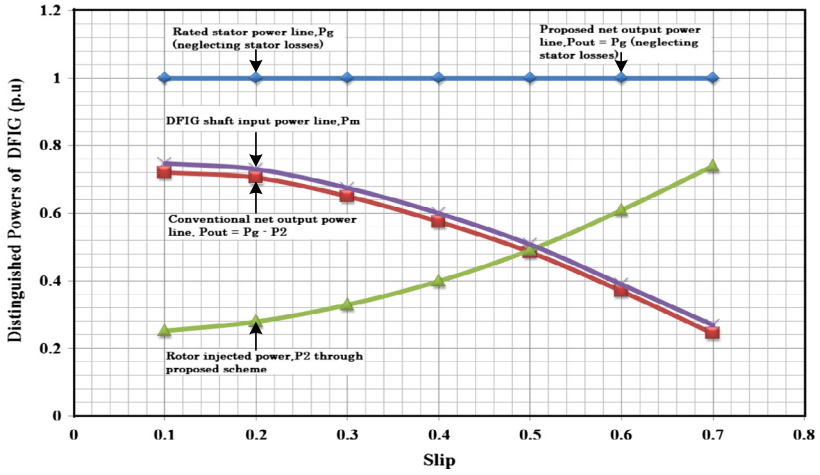

Fig. 2c. Power distribution of the proposed and existing conventional schemes.

generated electrical power at stator terminals is measured as $P_g = V^s_{\alpha s}.i^s_{\alpha s} + V^s_{\beta s}.i^s_{\beta s}$ in the stationary reference frame. Here both the rotor side inverter losses and stator copper and core losses are neglected for simplicity. The mechanical shaft power input is calculated using the formula $P_m = P_g - P_2$ as obtained from (8) after neglecting rotor copper losses. For each rotor speed, the corresponding P_g, P_2 and P_m are calculated. Then these powers are plotted as a function of slip as shown in Fig. 2c. From Fig. 2c, it can be observed that the injected rotor power steadily increases at increasing slip due to low shaft power input. The net output power for the conventional scheme is obtained by subtracting the rotor injected power P_2 from the power output P_g at the stator side. It can be also observed that, for the proposed scheme, the net output power at the stator is always more than the rotor injected power taken from PV panel for any slip conditions. The same is in corroboration with the expression derived in (8). Ideally at unity slip condition, when the mechanical injected power is zero, the rotor injected power taken from PV panel will equal the stator power considering no losses in the machine.

Comparing the proposed scheme with a classical topology of wind-solar hybrid generation as shown in Fig. 2d, where wind power generation and solar power generation is considered as two individual operators, the following advantages of the proposed scheme can be outlined.

- Unlike the proposed scheme, the alternate topology shown in Fig. 2d, suffers from complications of having another two converters i.e. grid side converter (GSC) and the inverter transformer unit connected to solar PV system. This will increase the overall cost of the system. This can also result in additional losses ranging up to 3–4% of the total output. Thus the overall efficiency of the proposed scheme can be higher by 3–4% compared to the alternate topology shown in Fig. 2d. Moreover, the control of these additional converters depends on the grid conditions like voltage unbalance, voltage swell or sag etc.
- The proposed scheme can be a more versatile option in comparison with the topology shown in Fig. 2d when grid isolated operation is considered.

Rotor position and speed estimation model

The proposed scheme accurately estimates the rotor position and speed required for precision control without any significant dependency on machine parameters at all operating condition. The reference model has been developed based on the measured values of the stator inputs in stationary reference frame as shown in Fig. 3, whereas the adjustable model torque requires the measured stator inputs and the rotor current transformed to the stationary reference frame using rotor position angle.

The reference model torque (T^*_e) in the stationary reference frame can be expressed as,

$$T^*_e = (3p/2)\left(\lambda^s_{\alpha s} i^s_{\beta s} - \lambda^s_{\beta s} i^s_{\alpha s}\right) = K_1\left(\lambda^s_{\alpha s} i^s_{\beta s} - \lambda^s_{\beta s} i^s_{\alpha s}\right) \tag{9}$$

where, 'p' is the number of poles, $K_1 = (3p/2)$ is a constant and superscript 's' denotes that the variables are in stationary reference frame. With $v^s_{\alpha s}$, $v^s_{\beta s}$ being the measured values of stator voltages in stationary $(\alpha s - \beta s)$ reference frame, the equations for stator flux linkages $\lambda^s_{\alpha s}$, $\lambda^s_{\beta s}$ can be expressed as,

$$\lambda^s_{\alpha s} = \int \left(v^s_{\alpha s} - R_s i^s_{\alpha s}\right) dt \tag{10}$$

$$\lambda^s_{\beta s} = \int \left(v^s_{\beta s} - R_s i^s_{\beta s}\right) dt \tag{11}$$

From (9)–(11) it can be observed that, T^*_e is independent of L_m and is computed from measured quantities. The relationship between rotor current in stationary and rotor reference frame can be written as,

$$\begin{bmatrix} i^s_{\alpha r} \\ i^s_{\beta r} \end{bmatrix} = \begin{bmatrix} \cos\theta_r & -\sin\theta_r \\ \sin\theta_r & \cos\theta_r \end{bmatrix} \begin{bmatrix} i^r_{\alpha r} \\ i^r_{\beta r} \end{bmatrix} \tag{12}$$

Thus, the measured rotor currents in rotor reference frame can be transformed to stator reference frame when the position of the rotor axis θ_r with respect to stationary αs axis is known.

The stator flux also can be determined using stator and rotor currents as,

$$\begin{bmatrix} \lambda^s_{\alpha s} \\ \lambda^s_{\beta s} \end{bmatrix} = L_s \begin{bmatrix} i^s_{\alpha s} \\ i^s_{\beta s} \end{bmatrix} + L_m \begin{bmatrix} i^s_{\alpha r} \\ i^s_{\beta r} \end{bmatrix} \tag{13}$$

Again, from stator flux Eq. (13),

$$\begin{bmatrix} i^s_{\alpha s} \\ i^s_{\beta s} \end{bmatrix} = \frac{1}{L_s} \begin{bmatrix} \lambda^s_{\alpha s} \\ \lambda^s_{\beta s} \end{bmatrix} - \frac{L_m}{L_s} \begin{bmatrix} i^s_{\alpha r} \\ i^s_{\beta r} \end{bmatrix} \tag{14}$$

Substituting $i^s_{\alpha s}, i^s_{\beta s}$ from (14) in (9), the adjustable model torque can be expressed as,

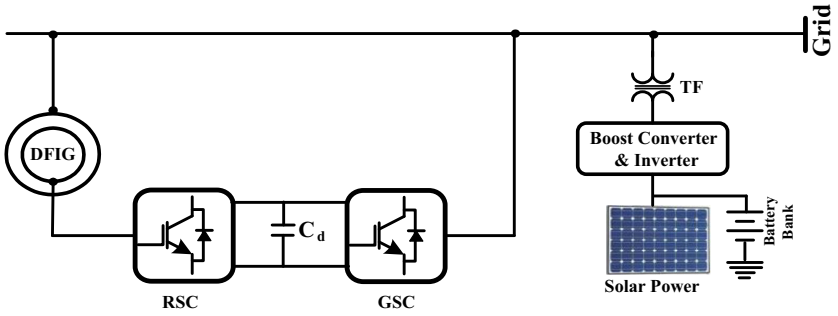

Fig. 2d. Classical topology of wind-solar hybrid generation.

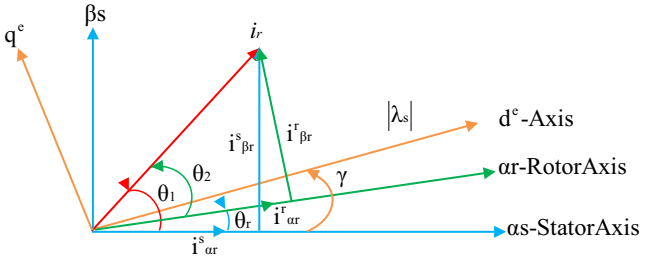

Fig. 3. Distribution of stator and rotor space vectors.

$$\widehat{T}_e = (-L_m/L_s)K_1\left(\lambda^s_{\alpha s} i^s_{\beta r} - \lambda^s_{\beta s} i^s_{\alpha r}\right) \tag{15}$$

Substituting $L_m = (1-\sigma s)L_s$ in (15),

$$\widehat{T}_e = (-K_1)(1-\sigma_s)\left(\lambda^s_{\alpha s} i^s_{\beta r} - \lambda^s_{\beta s} i^s_{\alpha r}\right) \tag{16}$$

where $\sigma_s = L_{ls}/L_s$, is the stator leakage factor.

Expression (16) gives adjustable model torque as a function of stator flux, rotor current in stationary reference frame. As σ_s is very close to zero and hence little variations with L_m , the adjustable model torque $\widehat{T}_e$ in (16) is almost insensitive to the variation in magnetizing inductance L_m of DFIG throughout the operation, unlike the existing techniques [6–16]. The influence of R_s in the stator flux computation is not significant, as the resistive voltage drops in (10) and (11) are negligible in practice under rated stator voltage. The implementation of the proposed MRAS is shown in Fig. 4. Thus using (9) and (16), when the rotor position θ_r is incorrect, an error ξ can be generated comparing T^*_e and $\widehat{T}_e$.

Thus the error ξ is expressed as,

$$\xi = T^*_e - \widehat{T}_e \tag{17}$$

The error ξ calculated using (17) is driven to zero through an adjustable mechanism designed by a PI controller. The output of adjustable mechanism is the estimated rotor speed which is integrated for rotor position θ_r and is used for demodulation of rotor currents $i^s_{\alpha r}, i^s_{\beta r}$.

a. Machine parameter sensitivity.

The parameter sensitivity of the algorithm for rotor speed and position estimation is analyzed and validated. It is evident that error in L_m leads to incorrect computation of adjustable model torque. Therefore variation in L_m will lead to error in the rotor position estimation. Referring to the Fig. 3;

$$\theta_2 = tan^{-1}\left(i^r_{\beta r}/i^r_{\alpha r}\right), \quad \theta_1 = tan^{-1}\left(i^s_{\beta r}/i^s_{\alpha r}\right) \tag{18}$$

Since, $i^r_{\alpha r}$ and $i^r_{\beta r}$ are the measured values of rotor current in rotor reference frame; the angle θ_2 remains unaffected from machine parameter variations. The angle θ_1 of rotor current phasor with respect to stationary αs axis. The estimation of θ_1 can be erroneous if computation of $i^s_{\alpha r}, i^s_{\beta r}$ or the estimation of rotor position is incorrect. Stator voltage components in the stationary reference frame can be expressed as;

$$v^s_{\alpha s} = R_s i^s_{\alpha s} + \left(d\lambda^s_{\alpha s}/dt\right), \quad v^s_{\beta s} = R_s i^s_{\beta s} + \left(d\lambda^s_{\beta s}/dt\right) \tag{19}$$

Aligning d-axis with stator flux in the synchronous rotating frame, the components of the stator flux in the stator stationary reference frame can expressed as;

$$\lambda^s_{\alpha s} = |\lambda_s|\cos\gamma, \quad \lambda^s_{\beta s} = |\lambda_s|\sin\gamma \tag{20}$$

where, 'γ' is a function of time and $d\gamma/dt = \omega_e$. Where, ω_e is expressed in rad./sec. From (20)

$$d\lambda^s_{\alpha s}/dt = [d|\lambda_s|/dt]\cos\gamma - \lambda^s_{\beta s}.\omega_e, \quad d\lambda^s_{\beta s}/dt = [d|\lambda_s|/dt]\sin\gamma + \lambda^s_{\alpha s}.\omega_e \tag{21}$$

Under constant stator flux operation, $d|\lambda s|/dt$ can be neglected in (21) and therefore from (19),

$$v^s_{\alpha s} = R_s i^s_{\alpha s} - \omega_e \lambda^s_{\beta s} = R_s i^s_{\alpha s} - \omega_e\left(L_s i^s_{\beta s} + L_m i^s_{\beta r}\right) \tag{22}$$

$$v^s_{\beta s} = R_s i^s_{\beta s} + \omega_e \lambda^s_{\alpha s} = R_s i^s_{\beta s} + \omega_e\left(L_s i^s_{\alpha s} + L_m i^s_{\alpha r}\right) \tag{23}$$

From (22), $i^s_{\beta r}$ and from (23), $i^s_{\alpha r}$, can be expressed as,

$$i^s_{\alpha r} = \left(v^s_{\beta s} - (R_s) i^s_{\beta s} - \omega_e L_s i^s_{\alpha s}\right)/\omega_e L_m \tag{24}$$

$$i^s_{\beta r} = \left(-v^s_{\alpha s} - (R_s) i^s_{\alpha s} - \omega_e L_s i^s_{\beta s}\right)/\omega_e L_m \tag{25}$$

To test sensitivity of R_s, let the change in R_s is ΔR_s so that new stator resistance is $R_s + \Delta R_s$. This can affect the estimation of$\hat{\theta}_r$, which in turn gives erroneous of $i^s_{\alpha r}, i^s_{\beta r}$. Considering the value of new rotor currents to be $(i^s_{\alpha r} + \Delta i^s_{\alpha r})$ and $\left(i^s_{\beta r} + \Delta i^s_{\beta r}\right)$, (24) and (25) can be rewritten as,

$$i^s_{\alpha r} + \Delta i^s_{\alpha r} = \left(v^s_{\beta s} - (R_s + \Delta R_s) i^s_{\beta s} - \omega_e L_s i^s_{\alpha s}\right)/\omega_e L_m \tag{26}$$

$$i^s_{\beta r} + \Delta i^s_{\beta r} = \left(-v^s_{\alpha s} - (R_s + \Delta R_s) i^s_{\alpha s} - \omega_e L_s i^s_{\beta s}\right)/\omega_e L_m \tag{27}$$

Subtracting (24) from (26),

$$\Delta i^s_{\alpha r} = [(-\Delta R_s)/(\omega_e L_m)] i^s_{\beta s} \tag{28}$$

Similarly from (25) and (27),

$$\Delta i^s_{\beta r} = [(\Delta R_s)/(\omega_e L_m)] i^s_{\alpha s} \tag{29}$$

In (28) and (29), $\Delta R_s \ll \omega_e L_m$ at rated stator frequency and therefore $\Delta i^s_{\alpha r}$ and $\Delta i^s_{\beta r}$ are very small. The new angle θ_1 will be;

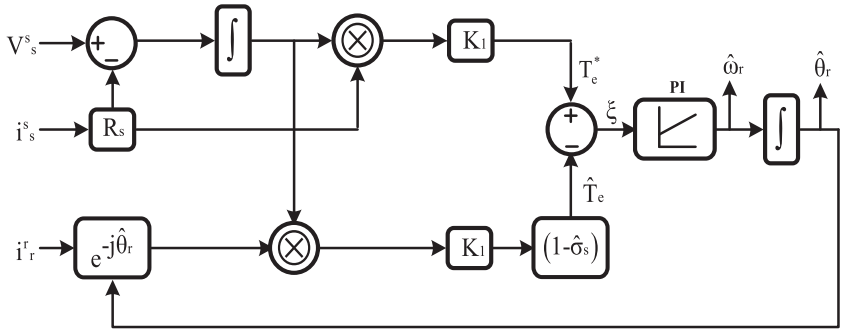

Fig. 4. Basic structure of the proposed estimator.

$$\theta_1 = tan^{-1}\left[(i^s_{\beta r} + \Delta i^s_{\beta r})/(i^s_{\alpha r} + \Delta i^s_{\alpha r})\right] \approx tan^{-1}\left[i^s_{\beta r}/i^s_{\alpha r}\right] \quad (30)$$

Considering (18) and (30), it is observed that the effect of R_s variation on rotor position estimation is insignificant for the proposed technique. The simulated variation of ξ and position error are shown in Figs. 5a and 5b respectively and change in ξ and estimated rotor position is negligible against +50% variations in R_s.

For most of the existing techniques, the adjustable variables used for rotor position estimation are rotor current, stator flux or rotor flux. These adjustable variables can be expressed as,

i. Rotor current, $\hat{i}_r = \frac{\lambda_s - L_s i_s}{L_m} e^{-j\hat{\theta}r}$,
ii. Stator flux, $\hat{\lambda}_s = L_s\left(i_s + \frac{L_m}{L_s}\right) i_r$ and,
iii. Rotor flux $\hat{\lambda}_r = L_r\left(i_r + \frac{L_m}{L_r}\right) i_s$.

From the above equations, the adjustable variables are directly sensitive Lm variations. The direct sensitivity of the adjustable variables with Lm will considerably affect the performance of the DFIG controller as the same usually varied during DFIG operation. In proposed control scheme, the adjustable variable $\widehat{T}_e$ seen from (16) is very weakly coupled to L_m. From (16), the term directly related with L_m is $(1-\sigma_s)$. For a any variation ΔL_m, the new magnetizing inductance is given by $(L_m + \Delta L_m)$. Therefore, $(1-\sigma_s)$ can modified as,

$$(1-(\sigma_s + \Delta\sigma_s)) = \frac{(L_m + \Delta L_m)}{(L_m + \Delta L_m + L_{ls})} = \frac{\left(1 + \frac{\Delta L_m}{L_m}\right)}{\left(1 + \frac{\Delta L_m + L_{ls}}{L_m}\right)} \quad (31)$$

It is observed that the maximum variations of $(1-\sigma_s)$ are +1.23% and −1.2% for L_m deviations of +50% and −50%. If Lm changes, torque will change. However, the change in the adjustable variable $\widehat{T}_e$ in the proposed scheme is negligible which provides more accurate estimation of rotor position which improves the subsequent controller actions.

For a L_m variation of ±50%, the variations in position error are shown in Fig. 6 and found almost negligible. The variation of leakage inductance is not considered in the present scheme which can also affect σ_s variation. For more precise calculation, the variation of leakage inductance with the stator flux can be obtained as shown [17] during commissioning phase and can be utilized for online applications.

The proposed torque based MRAS estimator for computation of rotor position is compared with already known MRAS techniques with different adjustable variables for the L_m variation between −50% to +50%. In Fig. 7, the rotor position angle errors for the L_m variation between −50% to +50% for various MRAS techniques including the proposed method are shown. It is observed that the proposed technique is superior with reduced sensitivity to L_m.

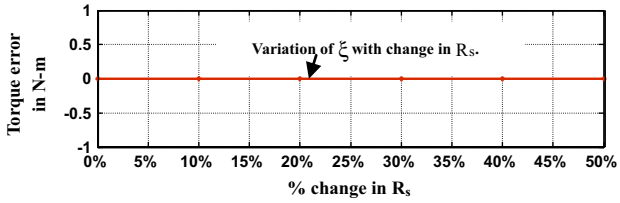

Fig. 5a. Variation of $\widehat{T}_e$ with change in R_s.

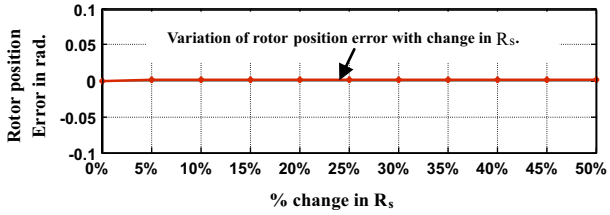

Fig. 5b. Variation in $\hat{\theta}_{error}$ rotor position with change in R_s.

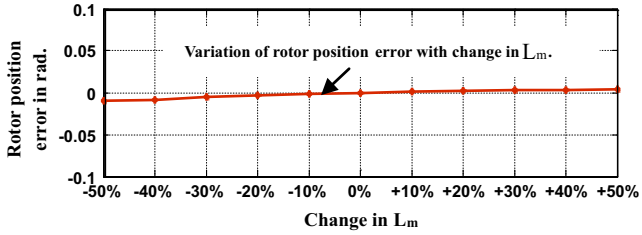

Fig. 6. Variation in rotor position error with change in L_m.

b. Stability analysis of the rotor speed and position estimator.

Stability of the system is analyzed when PI controller is used for stator reference frame.

Assuming, $\sigma_s \approx 0$, (16) can be written as,

$$\widehat{T}_e = (-K_1)\left(\lambda^s_{\alpha s} i^s_{\beta r} - \lambda^s_{\beta s} i^s_{\alpha r}\right) = (-K_1)[\lambda_s \otimes I_r] \quad (32)$$

With μ as the space angle between λ_s and I_r,

$$\widehat{T}_e = (-K_1)[\lambda_s I_r \sin(\mu)] \quad (33)$$

Assuming a disturbance of $\Delta\theta_r$ in estimation of rotor position θ_r, the new space position angle between λ_s and I_r will be $\mu + \Delta\theta_r$. This will modify the estimated torque $\widehat{T}_e$ to $\widehat{T}_e + \Delta\widehat{T}_e$.

From (33),

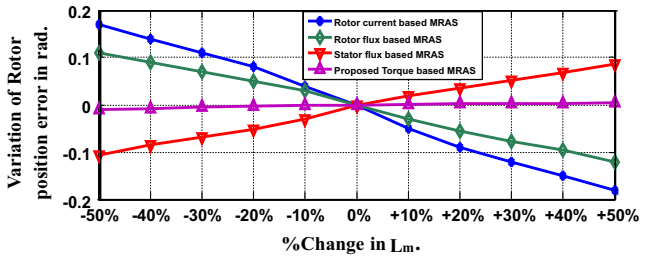

Fig. 7. Variation in $\hat{\theta}_{error}$ with change in L_m.

$$\hat{T}_e + \Delta\hat{T}_e = (-K_1)[\lambda_s I_r \sin(\mu + \Delta\theta_r)] = (-K_1)\lambda_s I_r[\sin\mu.\cos(\Delta\theta_r) + \cos\mu.\sin(\Delta\theta_r)] \quad (34)$$

For $\Delta\theta_r$ to be small,

$$\hat{T}_e + \Delta\hat{T}_e = (-K_1)\lambda_s I_r[\sin\mu + \Delta\theta_r.\cos\mu] \quad (35)$$

The difference between (35) and (33) can be expressed as,

$$\Delta\hat{T}_e = (-K_1)\lambda_s I_r[\cos\mu]\Delta\theta_r \quad (36)$$

The small-signal model for stability analysis is as shown in Fig. 8. From the transfer function of the PI-controller, the variable T_i has been defined as $T_i = K_p/K_i$. The delay introduced by sampling is represented by a first order system with τ_s as the time constant of the delay introduced by sampling.

Therefore from Fig. 8,

$$\xi = K_1\lambda_s I_r[\cos\mu]\Delta\theta_r \quad (37)$$

For the determination of PI controller parameters, symmetrical optimum control method is adopted [14,24]. The value of the K_p and T_i are selected such that the Bode magnitude and phase plot of open loop transfer function of the system shown in Fig. 8 are symmetrical about the gain crossover frequency ω_c, which is the geometric mean of the corner frequencies $(1/\tau_s)$ and $(1/T_i)$ of the open loop transfer function. Maximum phase margin can be ensured through symmetrical optimum method. This property is significant for the systems that have delays since the systems reaction to the change is retarded. Maximization of phase margin for a given bandwidth is desired due to system tolerance to more delays. With a normalized factor '*a*', $\omega_c = 1/a\tau_s$, $T_i = a^2\tau_s, K_p = 1/a\omega_0\tau_s$. In order to achieve stability, disturbance rejection and proper damping in the system, the parameter '*a*' must be appropriately selected. From Fig. 8, the characteristic equation is given by;

$$T_i\tau_s S^3 + T_i S^2 + (-K_1\lambda_s I_r K_p\omega_0 T_i\cos\mu)S + (-K_1\lambda_s I_r K_p\omega_0\cos\mu) = 0 \quad (38)$$

The array of coefficients of the characteristic equation in (38) can be expressed as;

S^3	$T_i\tau_s$	$-K_1\lambda_s I_r K_p\omega_0 T_i\cos\mu$
S^2	T_i	$-K_1\lambda_s I_r K_p\omega_0\cos\mu$
S^1	$-K_1(T_i-\tau_s)\lambda_s I_r K_p\omega_0 cos\mu$	0
S^0	$-K_1\lambda_s I_r K_p\omega_0 cos\mu$	0

Applying Routh-Hurwitz stability criterion with a constraint; $Ir \neq 0, Vs \neq 0$, the condition for stability is;

$$-K_1(T_i-\tau_s)\lambda_s I_r K_p\omega_0 cos\mu > 0 \quad (39)$$

$$-K_1\lambda_s I_r K_p\omega_0 cos\mu > 0 \quad (40)$$

To comply the stability criterion, from (39) and (40); $K_p\cos\mu < 0, T_i - \tau_s > 0$. As $K_p > 0, \cos\mu < 0$ for I_r positive and $\cos\mu > 0$ for I_r negative with $T_i - \tau_s > 0$. Here, μ varies within the specified range for rotor speed from subsynchronous to supersynchronous including synchronous speed at all loads. For the stability condition $T_i - \tau_s > 0, T_i > \tau_s$. As $T_i = a^2\tau_s$, the normalized factor $a > 1$ for $T_i > \tau_s$ [24].

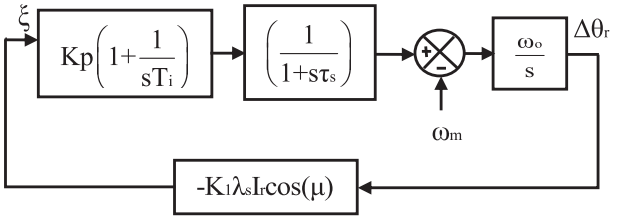

Fig. 8. The small signal model of the proposed estimator with PI controller.

The damping ratio; δ can be expressed as;

$$\delta = (a-1)/2 \quad (41)$$

Damping of the system depends on the choice of '*a*'. Moreover the value of δ could be 1 for critical damping and therefore, for $\delta = 1$ the value of $a = 3$. For the case of under damped system, assuming $\delta = 0.707$, the value of '*a*' can be obtained from (41) as $a = 2.41$. Thus properly adjusting '*a*', the system damping or bandwidth can be selected. For the present experiment, with critically damped system, $\delta = 1$ is taken for which $a = 3$ from (41). By changing the value of '*a*', the system damping or band width can be adjusted as required [14].

Selection of optimized rotor power storage capacity

For calculation of battery storage capacity both the wind and solar energies are taken into consideration. The average availability of solar power is assumed to be between 9 a.m. to 4 p.m. as shown in Fig. 9. The capacity of solar unit is so considered that it can deliver power both to DFIG rotor and for battery charging during day time and low wind speed situations. Considering the maximum slip up to 0.5 and average slip of 0.3 for the 2.5 kW generator both in subsynchronous and supersynchronous region, an average value of 0.75 kW of electrical power exchange will occur at the rotor terminals of the generator. Therefore, a 1.5 kW capacity of solar unit is considered to cope up the situation of both the charging of the battery and supplementing power to DFIG rotor during subsynchronous operation. The same will result in a battery capacity of 50Ah considering an average battery voltage of 144 V when the charge–discharge cycle given in Fig. 9 is considered. However, the design of solar unit and capacity of battery can be modified for different locations and considering different operation cycles.

Based on the cycle considered in Fig. 9, the overall size and cost of the proposed scheme can be calculated as,

- Total generated power = 2.5 kW × 24 h = 21,900 units/annum.
- Total AH of battery capacity required at battery voltage of 144 V = 50 Ah.
- The total cost of battery = $ 600 with 5 years of life.
- The cost of 1.5 kW solar panel @ $ 1/W = $ 1500 with 20 years of life.
- The cost of 2.5 kW DFIG and wind turbine = $ 500 with 20 years of life.
- The cost of converter with controller = $ 500 with 20 years of life.
- Considering depreciation, interest of 10% and 2% maintenance cost, total cost of generated energy per year = $ 617.
- Therefore, the unit cost of energy (COE) produced for the proposed scheme = $ 617/21900 = $ 0.028, which is well below the selling price $ 0.1/unit(approx.).

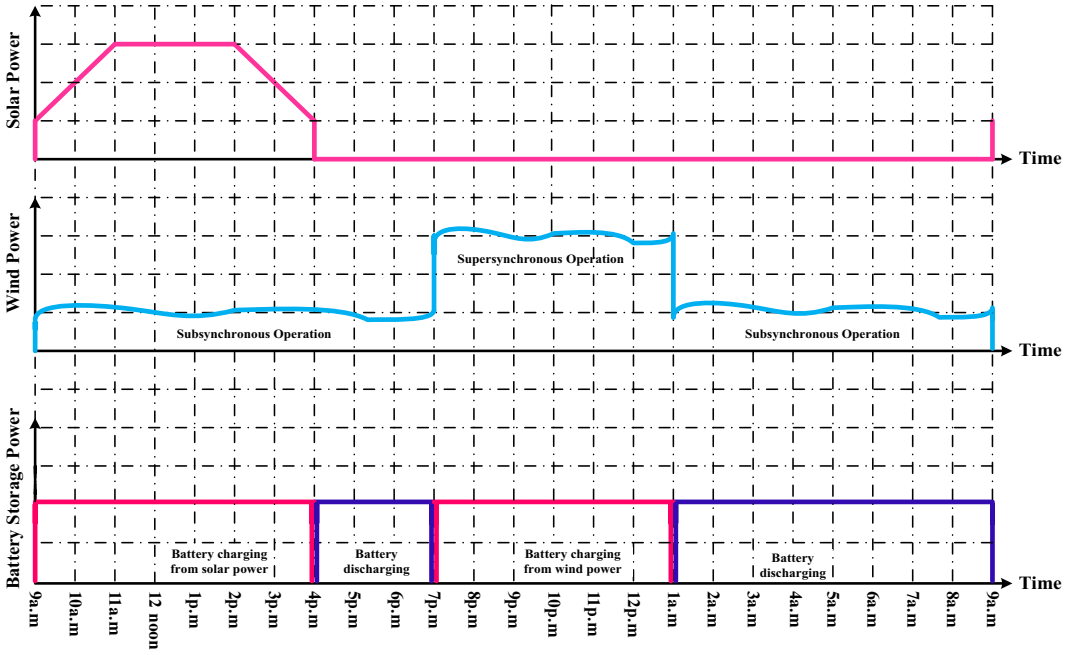

Fig. 9. Local energy input profile of the proposed wind-solar hybrid system.

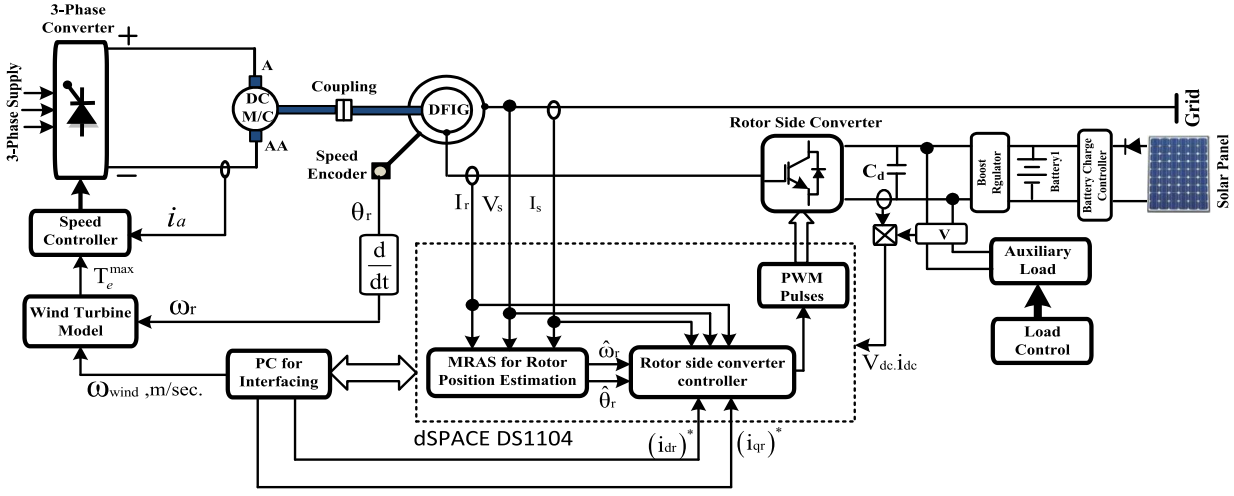

Fig. 10. Schematic diagram for validation of the proposed controller.

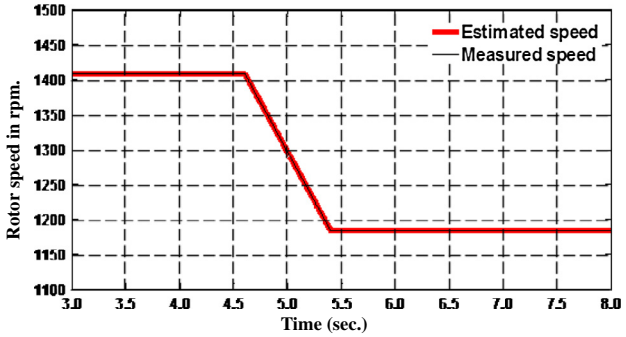

Fig. 11a. Transition of rotor speed in subsynchronous region.

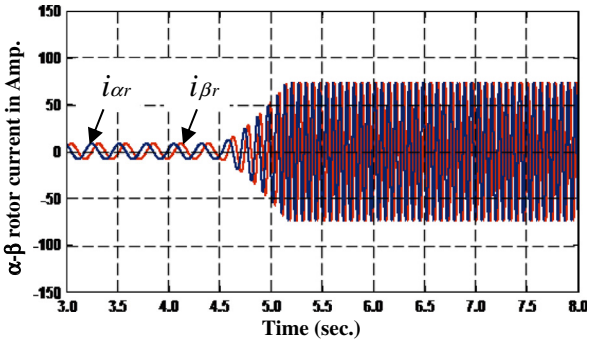

Fig. 11b. Nature α–β rotor current corresponding to Fig. 11a.

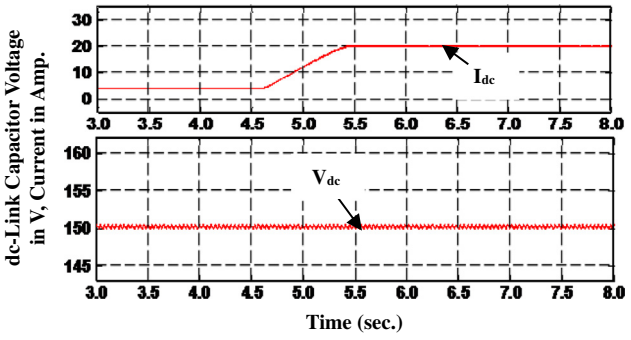

Fig. 11c. V_{dc} and I_{dc} corresponding to Fig. 10(a).

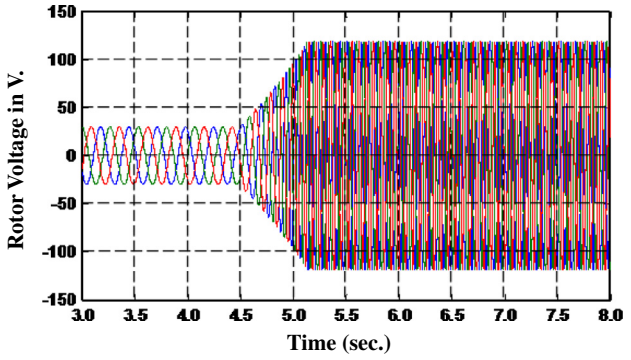

Fig. 11d. V_r corresponding to Fig. 11a.

The same data input was provided for verification using software tool HomerPro-3.2 and the unit cost of energy (COE) calculated through the software was $0.025 which justifies the calculations provided.

Experimental results

The proposed control scheme is implemented using a 2.5 kW, wound rotor induction machine working as DFIG. A 3.5 kW, 1500 rpm, dc separately excited motor with necessary torque control arrangement is coupled to the induction machine can emulate the wind turbine. A closed loop torque controller is used for the separately excited dc machine incorporating the wind turbine model. The shaft encoder gives the information regarding the speed of the shaft for the control of the dc machine. The experimental arrangement is shown in Fig. 10, where the measured values of stator voltage, stator current and rotor currents are fed to the controller as inputs. The stator and rotor currents sensed through LEM make Hall effect sensors LTS25NP while the voltage sensing is implemented through LEM make sensors CV3-1000.

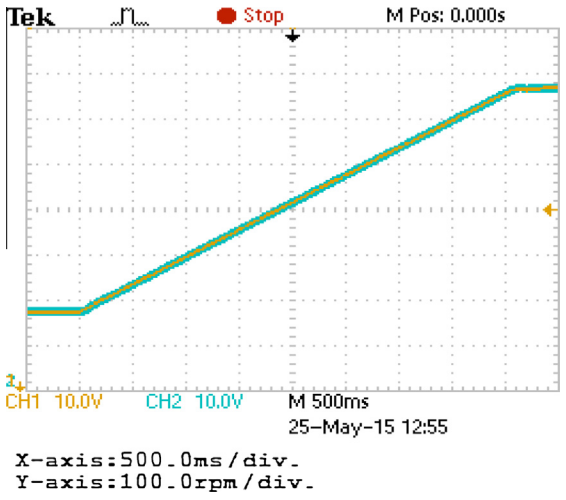

Fig. 12a. Variation in estimated rotor speed during rotor transition from subsynchronous to supersynchronous region with time.

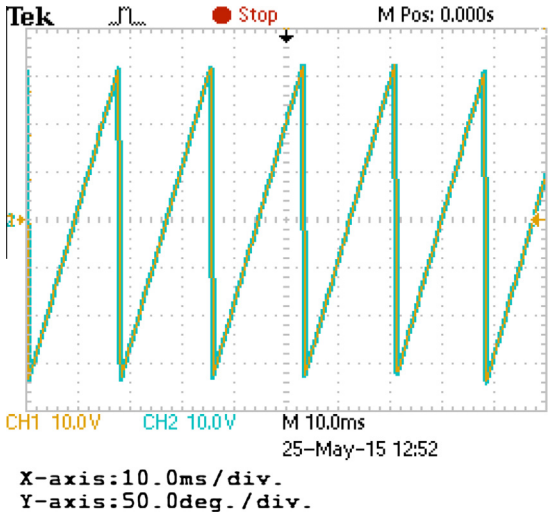

Fig. 12b. Variation in rotor position corresponding to Fig. 12a near synchronous speed with time.

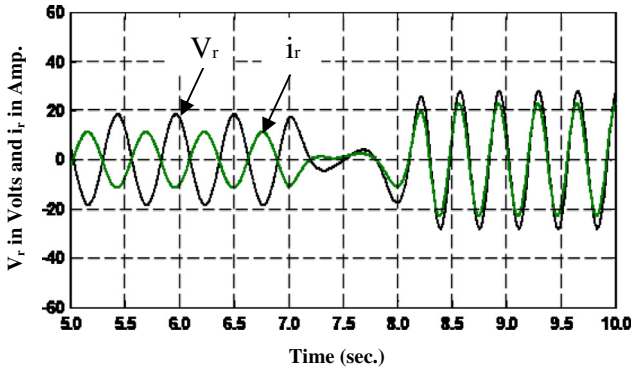

Fig. 12c. Variation of rotor voltage and current with time.

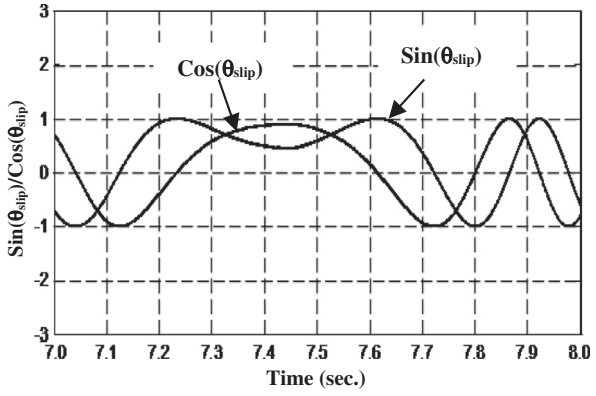

Fig. 12d. Variation in $\mathrm{Sin}(\theta_{slip})$ and $\mathrm{Cos}(\theta_{slip})$ with time.

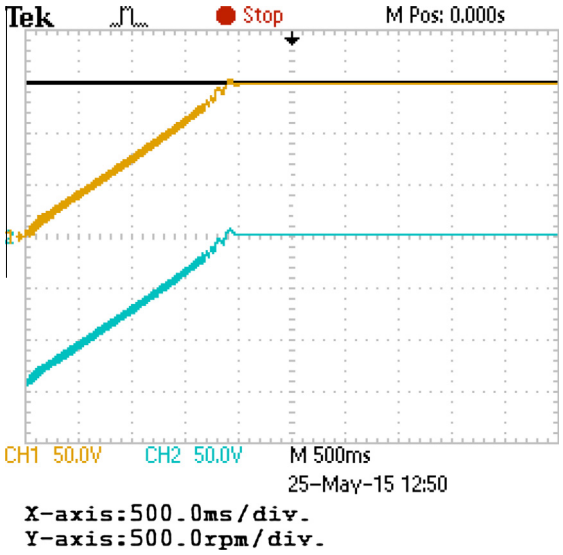

Fig. 13a. Estimated rotor speed catch to the reference.

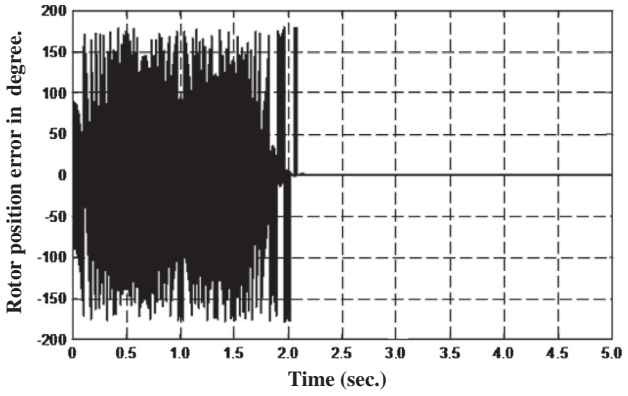

Fig. 13b. Error associated in estimation of rotor position angle during speed tracing.

A dSPACE DS1104 module with a PC interface is used for implementation of the experimental system.

Initially the machine was running at 1410 rpm with the help of the dc motor drive system. Then the speed was slowly reduced to 1185 rpm in 1second. The estimated speed through the proposed controller and the corresponding measured speed is shown in Fig. 11a while the rotor currents, dc bus voltage and current and the rotor voltages shown in Figs. 11b–11d respectively. It can be observed from Fig. 11c, for the dc-link capacitor voltage is maintained at 150 V during this period while dc-link current increases with decrease of speed or increase of slip. It can be also observed from Figs. 11b and 11d as the rotor injected power is to increase at high slip, both the rotor current and voltage has increased during this period.

Then in the next step, the rotor speed was increased from 1275 rpm to 1775 rpm in 4 s. The corresponding reading and estimated speed are shown in Fig. 12a. The measured and estimated rotor position at near synchronous speed are shown in Fig. 12b. Ii can be observed Figs. 11 and 12 that the proposed controller accurately estimates both the rotor position and speed during the speed transient. Fig. 12c shows the variation of rotor voltage and current when the rotor speed is crossing synchronous speed. The rotor current i_r and rotor voltage V_r are displaced in space almost 175° in subsynchronous region while 5° in supersynchronous region describing the reversal of rotor power. The corresponding behavior of sin and cosine of slip angle which is used for demodulating the rotor voltage and current signal is shown in Fig. 12d.

Then to check the grid connection, the speed tracking operation of the DFIG is performed with stator connected to utility grid and the prime mover speed adjusted at 1500 rpm. Fig. 13a shows the speed catching performance of the proposed scheme. It is observed that the speed error reduces to zero within 2 s from the starting of the rotor. The rotor position error varies between ±180° during this transition and is shown in Fig. 13b.

Conclusion

This paper describes a DFIG based wind-solar hybrid system as energy conversion mechanism. The rotor power is fed from a PV based converter system while the stator is directly connected to grid. The rotor is also coupled with a wind turbine for wind energy conversion purposes. One of the major advantages of the proposed wind-solar hybrid scheme is the enhanced option for power generation during low wind speeds. The rating of the converter can be selected based on the desired maximum operating slip. The proposed scheme accurately calculates rotor speed and position required for precision control without any significant dependency on machine parameters at all operating condition. The proposed control algorithm can also be extended successfully for grid isolated operation of DFIG. The stability of the system over specified speed range is verified through analytically and is found satisfactory. The proposed method is simple and can be easily implemented through any already available drive compatible processors.

Appendix A: Parameters of the DFIG

Stator voltage: 415 V, Y connected, Power: 2.5 kW, Poles: 4, Rotor: 150 V, Y connected, Speed: 1500 rpm, $R_s = 0.4\ \Omega$, $R_r = 0.45\ \Omega$, $L_{ls} = 0.015$ H, $L_{lr} = 0.015$ H, $L_m = 0.44$ H.

References

[1] Datta R, Ranganathan VT. Decoupled control of active and reactive power for a grid connected doubly fed wound rotor induction machine without position sensors. In: IEEE conf. proc.; 1999. p. 2623–30.
[2] Datta R, Ranganathan VT. A simple position-sensorless algorithm for rotor-side field-oriented control of wound rotor induction machine. IEEE Trans Indust Electron 2001;48(4):786–93.
[3] Datta R, Ranganathan VT. Direct power control of grid connected wound rotor induction machine without rotor position sensors. IEEE Trans Power Electron 2001;16(3):390–9.
[4] Karthikeyan A, Nagamani C, Ray Chaudhury AB, Illango GS. Implicit position and speed estimation algorithm without the flux computation for the rotor side control of doubly fed induction motor drive. IET Electr Power Appl 2012;6(4):243–52.
[5] Karthikeyan A, Nagamani C, Illango GS. A versatile rotor position computation algorithm for the power control of a grid-connected doubly fed induction generator. IEEE Trans Energy Convers 2012;27(3):697–706.
[6] Cardenas R, Pena R, Proboste J, et al. MRAS observer for sensorless control of standalone doubly fed induction generators. IEEE Trans Energy Convers 2005;20(4):710–8.
[7] Cardenas R, Pena R. Sensorless vector control of induction machines for variable-speed wind energy applications. IEEE Trans Energy Convers 2004;19(1):196–205.
[8] Cardenas R, Pena R, Proboste J, et al. Rotor current based MRAS observer for doubly fed induction machines. IEEE Electron Lett 2004;40(12).
[9] Cardenas R, Pena R, Proboste J, et al. MRAS observers for sensor less control of doubly-fed induction generators. IEEE Trans Power Electron 2008;23(3):1075–84.
[10] Cardenas R, Pena R, et al. Sensorless control of doubly-fed induction generators using a rotor-current-based MRAS observer. IEEE Trans Industrial Electron 2008;55(1):330–9.
[11] Xu L, Cheng W. Torque and reactive power control of a doubly fed induction machine by position sensorless scheme. IEEE Trans Industry Appl 1995;31(3):636–42.
[12] Marques GD, Sousa DM. New sensorless rotor position estimator of a DFIG based on torque calculations-stability study. IEEE Trans Energy Convers 2012;27(1):196–203.

[13] Marques GD, Sousa DM. Sensorless direct slip position estimation of a DFIM based on the air gap pq vector-sensitivity study. IEEE Trans Indust Electron 2013;60(6):2442–50.
[14] Marques GD, Pires VF, Sousa S, et al. A DFIG rotor-position detector based on a hysteresis controller. IEEE Trans Energy Convers 2011;26(1):9–17.
[15] Marques GD, Sousa DM. Air-gap-power-vector-based sensorless method for DFIG control without flux estimator. IEEE Trans Indust Electron 2011;58 (10):4717–26.
[16] Marques GD, Sousa DM. A new sensorless MRAS based on active power calculations for rotor position estimation of a DFIG. In: Advances in power electronics. Hindawi Publishing Corporation; 2011. p. 1–7.
[17] Chatterjee D. A simple leakage inductance identification technique for three phase induction machines under variable flux condition. IEEE Trans Indust Electro 2012;59(11):4041–8.
[18] Farshadnia M, Teher SA. Current-based direct power control of a DFIG under unbalanced grid voltage. Int J Elect Power Energy Syst 2014;62:571–82.
[19] Rahimi M, Parniani M. Low voltage ride-through capability improvement of DFIG-based wind turbines under unbalanced voltage dips. Int J Elect Power Energy Syst 2014;60:82–95.
[20] Zandzade JM, Vahedi A. Modeling and improvement of direct power control of DFIG under unbalanced grid voltage condition. Int J Elect Power Energy Syst 2014;59:58–65.
[21] Shethata EG, Salama G. Direct power control of DFIGs based wind energy generation systems under distorted grid voltage conditions. Int J Elect Power Energy Syst 2013;53:956–66.
[22] Rashid MH. Power electronics circuits, devices, and applications. 3rd ed. Pearson Education; 2011. p. 727–38.
[23] Krause PC, Wasynczuk O, Sudhoff SD. Analysis of electric machinery and drive systems. 2nd ed. Wiley-IEEE Press; 2011. p. 141-17, 338–40.
[24] Leonhard W. Control of electrical drives. Springer; 2001. p. 281–326.